Current Science
CS 6 (4), 6473-6498 (2026)
Received 26 June 2026 | **Accepted 13 July** 2026 | **Online Available 14 July** 2026
https://doi.org/10.52845/CS/2026-6-4-7

Current Science

Current Science

OPEN ACCESS **ISSN(O)2795-8639**

Original Article

Three-Dimensional Geological Models (3D Gms) and Their Spatial Analysis Methods for Mineral Prospectivity Modelling (MPM)

Juxiang He[1], Yongran Wang[2], Xiaoxia Long[1], Bicheng Wang[2], Jinsong Yang[1], Kun Wu[2], Or Aimon Brou Koffi Kablan[3], And Lifang Wang[4,*]

[1]Yunnan Diqing Non-Ferrous Metal Co., Ltd., Diqing 674408, China

[2]Kuming Prospecting Design Institute of China Nonferrous Metals Industry Co., Ltd., Kunming 650051, China

[3]School of Geosciences and Info-Physics, Central South University, Changsha 410083, China

[4]Department of Surveying and Mapping Geography, Hunan Vocational College of Engineering, Changsha 410151, China

***Corresponding Author: Lifang Wang**

Abstract:
A comprehensive review of three-dimensional geological models (3D GMs) and their spatial analysis and statistics methods for mineral prospectivity modeling (MPM) is presented. Firstly, we explore both explicit and implicit 3D geological modeling techniques and examine data structures of 3D GMs. The primary challenge of representing and modeling complex geological structures remains still unresolved. The ultimate objective of 3D geological modeling is to facilitate further spatial analysis and practical applications. Thus, constructing 3D GMs with essential geological characteristics necessitates the abstraction, selection, and integration of multi-resource data. Secondly, 3D GMs can undergo further spatial analysis and statistics methods within 3D geographical information systems (GIS). In the realm of geological variable construction, commonly employed spatial analysis methods include interpolation analysis, stochastic simulation, distance analysis, direction analysis, iso-surface analysis, gradient analysis, spatial auto-correlation analysis, and clustering analysis. Moreover, when investigating the relationships among geological variables, techniques such as cross-correlation analysis and spatial regression analysis are commonly employed.

Keywords: **3D geological model; Solid model; Volumetric model; Explicit modeling; Implicit modeling; Spatial statistics.**

Introduction

As digital mines mature and progress on their applied studies, the limitations of traditional two-dimensional (2D) information displaying becomes increasingly evident, especially in geological body representation (Cui et al., 2026; Wu et al., 2013). Growing needs to analyze and solve geological problems from a real 3D perspective pushes three-dimensional (3D) geological modeling to unprecedented strategic heights. Houlding (1994) introduced core theories and basic methods of 3D geological modeling in subsurface 3D visualization technology, including spatial database setting, triangulation methods, surface modeling, delineating and connecting geological boundaries, reserve calculation, and mining design. 3D geological modeling entails the establishment of mathematical models to express geological characteristics in appropriate computer data structures, e.g., the shapes of geological structures, the relationships among geological bodies, and the spatial distribution of geological bodies' physical and chemical properties. With advancement in geological exploration, revolutions in deep-penetration geophysical and geochemical explorations, and accumulation of multi-source geosciences databases, the prospect of studying geological bodies' geometries and properties from a 3D perspective becomes feasible (Hu et al., 2020; Wu et al., 2005; Zhang et al., 2023). The 3D geological modeling falls within the research field of visualization in scientific computing, rendering complicated concepts in intuitive graphics and images to help geologists understand phenomena, discover laws, and convey knowledge. The applications of 3D geological models (3D GMs) span four levels: visualization, spatial query, spatial analysis, and engineering practice, which play vital roles in conducting real 3D reconstruction and analysis of subsurface entities, e.g., strata, fault networks, intrusive rocks, geophysical and geochemical properties, orebodies, and related artificial structures (García-Gil et al., 2023; Lajaunie et al., 1997; Pan et al., 2020; Zhang et al., 2018). Its foundation lies in multi-source geosciences spatial databases, integrating data from different disciplines, sources, types, periods, and precisions. The process involves fusing multi-source geosciences spatial data, e.g., geological, geophysical, geochemical, and remote sensing data, in a unified 3D visualized environment. The outputs, 3D GMs, enables the investigation of the spatial distribution, orientation, and evolutionary relationship of geological bodies (Jessell, 2001; Zhang et al., 2023), serving as input of 3D visualized geosciences numerical simulations and further engineering applications. The rise of 3D geological modeling is gradually reshaping traditional geological works, which allows for the full utilization of geosciences data accumulated over time, indicating a new direction for constructing various geosciences spatial databases. In the foreseeable future, geological work submissions may transition from reports and maps to comprehensive 3D databases, including geological models and associated raw data.

The 3D mineral prospectivity modeling (MPM) serves as the predictive intelligence engine within digital mines, transforming multi-source geological data into probabilistic 3D targeting maps to guide exploration and reduce uncertainty in subsurface resource discovery (Li et al., 2023; Xie et al., 2025; Zhang et al., 2023). In 3D MPM, it is necessary to express the distribution of the intensity and trend of geological ore-controlling variables in the 3D space and to establish the spatial relationship model among 2D/3D and qualitative/quantitative geosciences data. Therein, spatial analysis and statistics methods applied to 3D GMs are useful tools for quantifying ore-controlling factors, extracting mineralization signatures, and constructing predictive algorithms in 3D MPM (Deng et al., 2022; Xu et al., 2021; Zhang et al., 2018). They extract deep information from 3D geological field models, including geological evolution, sub-surface geological structure, and mineralization (Bérubé et al., 2018; He et al., 2021). They are necessary for analyzing ore-forming environments, extracting effective ore-controlling factors, and describing real ore-forming processes in 3D MPM.

1 Geometric modeling

3D geological geometric modeling focuses on constructing reasonable solid models to represent the geometric shapes, topological relationships, and logic of subsurface geological bodies (Galley et al., 2020; Mallet, 2002). There are two kinds of 3D geological geometric modeling methods: explicit and implicit methods. The explicit method involves reconstructing geological boundaries, relying heavily on a time-consuming process of manual digitization. This method can be best described as surface modeling, which complex geological bodies are built up lying on the surfaces by digitizing lines and points. In contrast, implicit modeling does not explicitly reconstruct or digitize surfaces, whereas implicitly contains them within volumetric functions.

2.1 Explicit Modeling

The roadmap of 3D geological explicit modeling involves multi-source data, multi-method integration, and multi-level human-computer intervention (Chen et al., 2023; Mallet, 2002; Wu et al., 2005; Zhong et al., 2018). Explicit modeling provides a detailed representation of explicit boundaries, such as geological interfaces, digital elevation models (DEMs) and fault surfaces, which reconstructs a 3D vector model of geological bodies. Reconstructed surfaces can either form closed boundaries that encapsulate geological bodies, or remain open as fault surfaces. For instance, close surfaces may represent layered strata with defined top, bottom, and side boundaries. However, current explicit methods require a complicated and time-consuming human-computer interactions for connecting boundary lines, and it is difficult to update the model, hindering the widespread adoption of 3D geological modeling.

2.1.1 Multi-layer DEM

The multi-layer DEM method involves building the DEMs for all stratigraphic interfaces successively and then stitching them together on perimeters to form the stratigraphic model. It capitalizes on the fact that some stratigraphic interfaces can be represented as vertical single-valued surfaces, meaning that each horizontal (x, y) coordinate corresponds to a unique elevation value z (Hou et al., 2025; Kaufmann et al., 2008; Lemon et al., 2003). Interpolation or fitting of sampling points essentially determine a single-valued DEM function $z(x, y)$ for each stratigraphic interface, which is then represented using a triangulated irregular network (TIN). Similarly, perimeter boundaries where these interfaces are stitched together are also constructed and represented as TIN surfaces, which are foundational together with stratigraphic interfaces for constructing the model. All stratigraphic interfaces share an identical horizontal projection extent, with pinch-out zones specially treated as zero-thickness layers where the top and bottom interfaces coincide, as shown in Figure 1a. Integrating multi-layer DEM with tri-prism volume (TPV) facilitates voxelization of strata into irregular tri-prism grids, which offers the possibility of real 3D spatial analysis. Each corresponding pair of triangles from the top and bottom triangulated surfaces define the top and bottom facets of a tri-prism. The vertical edges of the tri-prism are formed by connecting the three corresponding vertices of these aligned triangular facets, as shown in Figure 1b. In an extended tri-prism, the top and bottom triangular facets can be non-parallel, and its three lateral edges can also be non-parallel, a geometric flexibility designed to accommodate the spatial configuration of actual sampling data, as shown in Figure 1c. Furthermore, with one to two its vertical edges degenerated to a vertex, or with the top or bottom triangle facets degenerated to an edge or a vertex, a tri-prism degenerates a pentahedron or a tetrahedron, which is treated specially in generalized tri-prism (GTP) (Houlding, 1994; Wu, 2004; Zhang et al., 2015). Guo et al. (2021) provided the process for subdividing a tri-prism and a pentahedron to generate the tetrahedron network (TEN) model. The coupled multi-layer DEM with TPV or TEN overcomes the limitation of 3D vector models being confined to visualization and spatial queries. However, multi-layer DEM struggle with complex geological structures such as reverse faults and recumbent folds, which created multi-valued interfaces, meaning that each horizontal coordinate corresponds to multiple elevation values, as well as with branching vein-type orebodies and sedimentary facies. Therefore, it is primarily suited for engineering geology applications in urban settings.

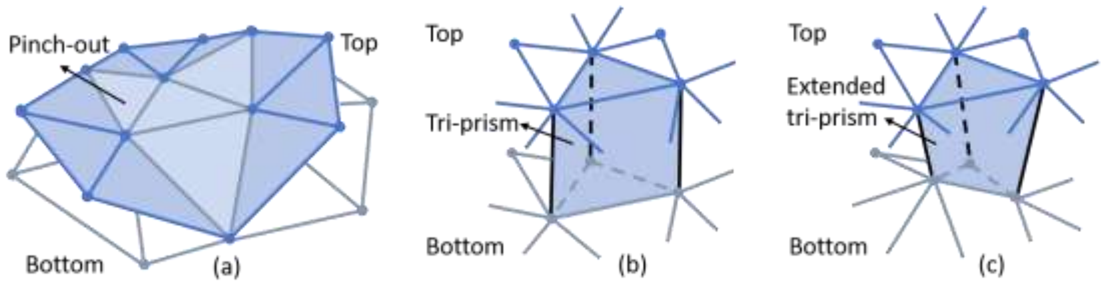

Fig. 1 (a) Multi-layer DEM treats pinch-out zones as zero-thickness layers, and it can be coupled with TPV model using (b) regular and (c) extended tri-prisms

2.1.2 Boundary-Representation

Geological structures often exhibit complex geometric boundaries that cannot be adequately described by the regular top, bottom, and side surfaces. To address this, the boundary-representation (B-Rep) method reconstructs geological bodies with multiple boundary surfaces such as fault surfaces, DEM, and geological interfaces (Liu et al., 2012; Tian et al., 2024; Wu et al., 2003; Zhong et al., 2018). It constructs a tectonic frame to delineate sub-regions, within which strata and intrusive rocks are subdivided into separated geological bodies (Wu et al., 2003). Subsequently, a boundary surface is subdivided into several sub-surfaces composed of triangular patches and shared boundary lines, while geological body is enclosed by multiple sub-surfaces that define its interfaces with adjacent bodies. In B-Rep, sub-surfaces are precisely represented as multi-valued TINs, which capture complex geometries with irregular triangles. The TINs often require densification to maintain favorable triangulation morphology; however, this process must avoid introducing geometric and topological inconsistencies at the junctions of sub-surfaces. Wu et al. (2005) proposed a fractal-based triangular recursive subdivision method, which iteratively calculates the midpoint of each triangle's edges and reconstructs new triangular patches to achieve effective densification. These TIN-constrained sub-surfaces then guide a tetrahedralization process that subdivides enclosed geological bodies into a non-overlapping TEN model, enabling robust 3D spatial analysis operations such as volume calculating, cutting, and heterogenous property representing. However, complex topological relationships in a 3D geological hybrid model must be maintained among geological bodies, tetrahedra, surfaces, sub-surfaces, and boundary lines.

In B-Rep, the global and the local approaches for reconstructing faulted stratigraphic interfaces present distinct trade-offs between geological fidelity and practical feasibility. The global approach offers the significant advantage of utilizing the complete dataset from both sides of the fault during the initial interpolation, thereby constructing a geologically consistent, pre-faulting stratigraphic interfaces that honor the original depositional or structural continuity. This leads to a more robust and realistic final model, as the subsequent separation and displacement based on fault geometry inherently maintain the stratigraphic correlation across the fault. However, it often requires computationally intensive structural restoration to approximate pre-faulting interfaces, relying on sometimes an uncertain tectonic restoration step (Mallet, 2004). In contrast, the local approach treats each fault block independently, simplifying the workflow by eliminating the need for complex tectonic restoration and avoiding cross-fault data interference. This makes it more straightforward and faster. Its primary disadvantage, however, is the potential loss of geological consistency; by ignoring data from the opposite block, the method may produce surfaces that do not align correctly across the fault or fail to honor the regional geological trend, especially when local data is sparse, leading to increased uncertainty and potential interpolation artifacts near the fault zone (Wu et al., 2003).

In geological practice, cross-sections serve as the primary means of visualizing and interpreting subsurface 3D geological structures. The contour lines on cross-sections, either closed or open, are the intersecting lines between cross-sections and geological bodies, as shown in Figure 2a. Within the B-Rep framework, cross-sections constitute a main data source, around which special modeling methods have been developed to reconstruct 3D geological bodies from 2D sectional contours. Utilizing 2D sectional contours to reconstruct 3D multi-valued surfaces, usually represented by TINs, faces three main challenges of corresponding, branching, and tiling of contours (Chen et al., 2023; Meyers et al., 1992; Xu et al., 2003). After a clear corresponding and branching wireframe among sectional contours is confirmed, usually with essential human-computer interaction, it can also be filled with TINs by tiling corresponding contours to form the model, as shown in Figure 2b. Roberto et al. (1999), Perrin et al. (2005) and Chen et al. (2023) used knowledge-driven and reasoning methods to build the wireframe among contours.

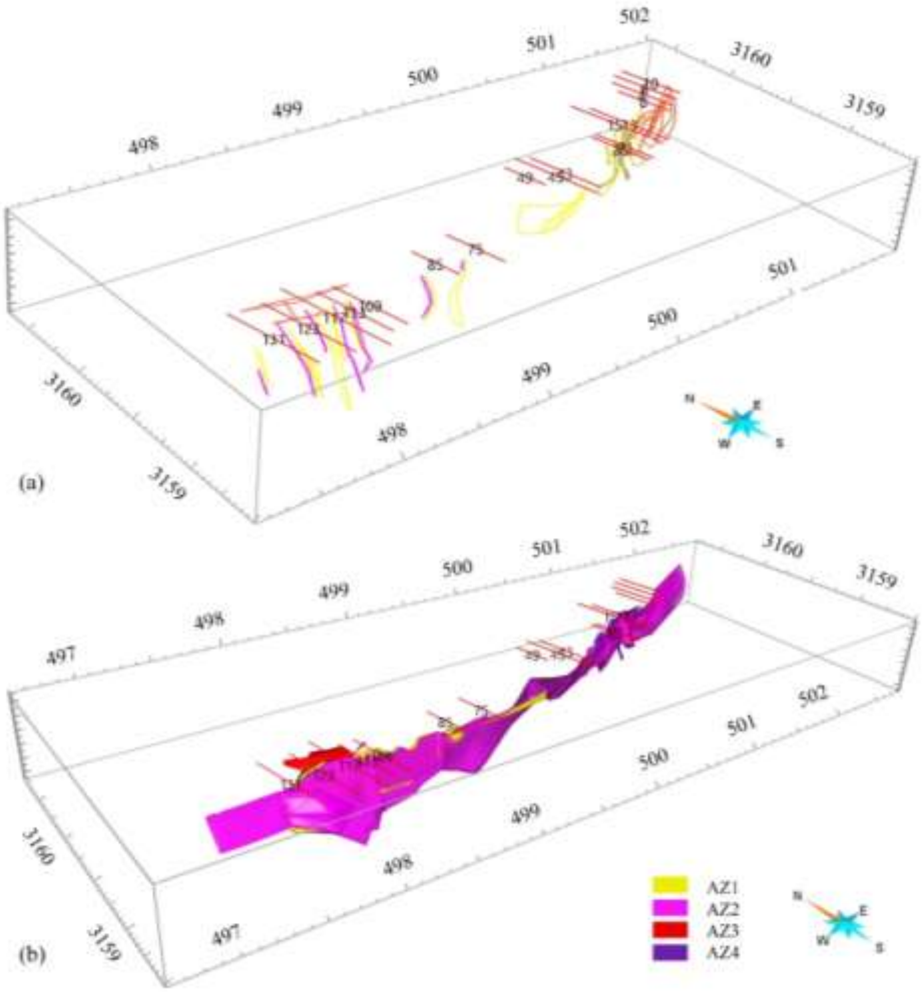

Fig. 2 (a) Sectional contours and (b) 3D GMs of hydrothermal alternation zones AZ1, AZ2, AZ3, and AZ4 in a gold deposit

2.1.3 TEN Modelling

TEN modeling employs irregular tetrahedra as elementary voxels to discretize 3D subsurface space, with irregular boundaries by enabling local refinement and topological optimization, enabling the faithful representation of complex geological bodies through adjacent and non-overlapping tetrahedra, while their outermost triangular facets effectively delineate smooth and continuous geological interfaces (Antepara et al., 2021; Si, 2015; Xue et al., 2004; Yusoff et al., 2022). It utilizes tetrahedralization of scattered sampling points to partition 3D subsurface space, requiring the additional constraints that triangles from geological interface TINs must serve as facets of the tetrahedra, and geological boundary lines must act as edges of the tetrahedra, as shown in Figure 3. TEN modeling enhances the accuracy of geological property interpolation, such as Kriging estimation, by providing a structurally constrained framework that incorporates the geometry of geological bodies (Feather et al., 2021). Its spatial discretization is inherently compatible with numerical simulation methods like finite element analysis, thereby improving the precision and reliability of geosciences numerical modeling (Feather et al., 2021; Li et al., 2019; Schneider et al., 2022; Tanaka et al., 2022).

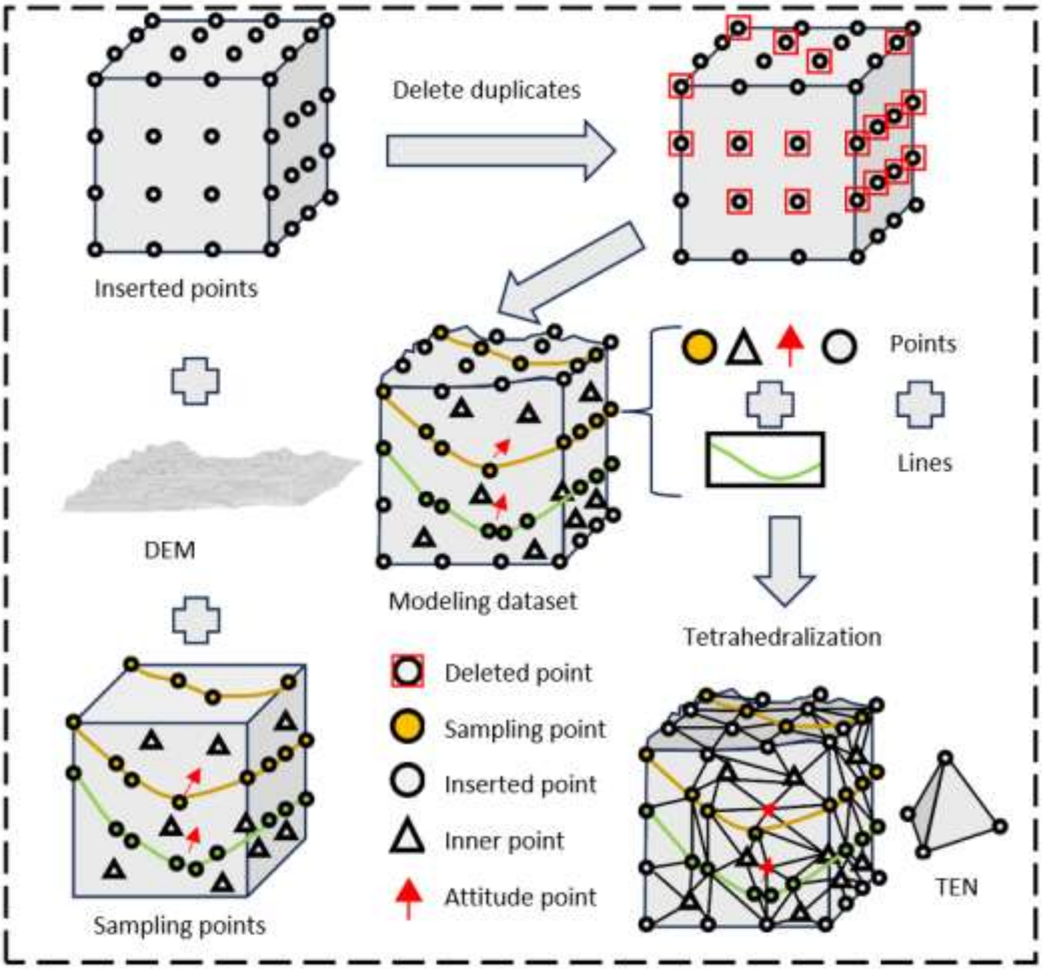

Fig. 3 Tetrahedralization under constraints of sampling points and geological boundary lines

2.2 Implicit Modeling

The key of implicit modeling methods is to interpolate a 3D volumetric function $f(\boldsymbol{p})$ at any point $\boldsymbol{p}$, which is interpolated from stratigraphic interface sampling points $\{(\boldsymbol{p}_i, f_i)\}_{i=1}^{N}$ and structural orientations $\{(\boldsymbol{p}_j, \nabla f_j)\}_{j=1}^{M}$, such as stratification or foliation, using either discrete or continuous interpolation schemes (Lajaunie et al., 1997; Mallet, 2004). Its values are set as grades of orebodies or relative eras of geological interfaces $\{f(\boldsymbol{p}_i) = f_i\}_{i=1}^{N}$, and structural orientations $\{\nabla f(\boldsymbol{p}_j) = \nabla f_j\}_{j=1}^{M}$ are treated as gradients of the volumetric function. Gradient, $\nabla f(\boldsymbol{p}_j) = \frac{\partial f}{\partial x}\hat{\boldsymbol{x}} + \frac{\partial f}{\partial y}\hat{\boldsymbol{y}} + \frac{\partial f}{\partial z}\hat{\boldsymbol{z}}$, is the most important microscopic characteristic of the volumetric function, reflecting the variation trend of the volumetric function in space. It represents the largest directional derivative in all directions at each point and is perpendicular to iso-surfaces. Hillier et al. (2013) presented a structural field interpolation (SFI) algorithm derived from eigen analysis of structural orientations. Implicit modeling allows for the automatic extraction of iso-surfaces from the volumetric function, $f(\boldsymbol{p})$ = const, as orebodies or geological interfaces, as shown in Figure 4. As the most important macroscopic characteristic of volumetric function, iso-surface is a surface formed by connecting points with the same constant volumetric function value. Since there are countless non-intersecting iso-surfaces in the volumetric function, orebodies and geological interfaces are those iso-surfaces of specific grades or relative geological eras. A stratum occupies the space between the top and bottom interfaces, and the volumetric function values inside a stratum change gradually from top to bottom. The increasing importance of implicit modeling stems from the advantages of efficiency, reproducibility and topological consistency (Cowan et al., 2003).

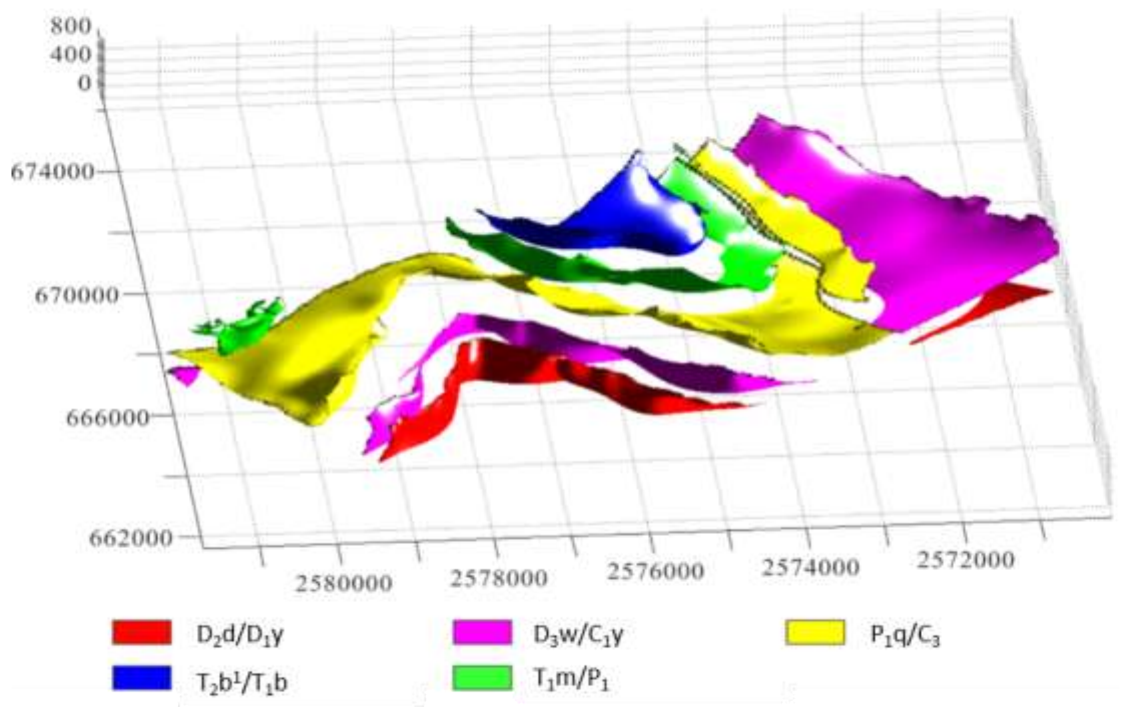

Fig. 4 Stratigraphic interfaces between the Donggangling Stage (D_2d) and the Yujiang Stage (D_1y), between the Wuzhishan Formation (D_3w) and the Yanguan Formation (C_1y), between the Qixia Formation (P_1q) and the Upper Series of Carboniferous (C_3), between the Majiaoling Formation (T_1m) and the Lower Series of Permian (P_1), and between the Lower Member of Baifeng Formation (T_2b^1) and Beisi Formation (T_1b) in a manganese deposit

The discrete interpolation schemes of implicit modeling rely on computational meshes, offering robustness in handling complex structures but at the cost of significant computational resources and sensitivity to mesh quality (Caumon et al., 2013; Grose et al., 2021; Irakarama et al., 2020; Mallet, 2004). Since the continuous interpolation schemes does not depend on a mesh for its definition, the extracted orebodies or geological interfaces can be extracted at any desired resolution in the specific volume of interest. There are already Kriging (Calcagno et al., 2008; de la Varga et al., 2019; Goncalves et al., 2017; Lajaunie et al., 1997) and radial basis function (RBF) (Basson et al., 2016; Cowan et al., 2003; Guo et al., 2021; Zhang et al., 2023) formulations for continuous implicit modeling of geological interfaces without a mesh. However, when the volume of modeling dataset scales up, the computational cost of solving large linear systems of interpolation increases significantly. Moreover, in geologically complex settings, needs of incorporating additional geological constraints, such as fault kinematics (Grose et al., 2021) and fold geometry (Frings et al., 2023), may complicate the governing equations and increase computational complexity.

Deep neural networks (DNNs) enable implicit modeling for geological interfaces without solving large systems of linear equations. Moreover, these methods mitigate the impact of global smoothness criteria on local model features and replace cumbersome constraint equations with learnable loss functions, thereby improving methodological flexibility. Due to their superior nonlinear representation capacity, multilayer perceptron (MLP) (Guo et al., 2024; Hillier et al., 2023), convolutional neural networks (CNNs) (Bi et al., 2022), and graph neural networks (GNNs) (Hillier et al., 2021) have become a prominent direction in 3D geological modeling.

2 Attribute Modeling

3D geological attribute modeling aims to characterize the complex and heterogeneous internal properties of geological bodies, primarily employing various spatial interpolation and stochastic simulation methods and typically utilizing volumetric models (Feather et al., 2021; Goovaerts, 1997; Isaaks et al., 1989; Martelet et al., 2004). The geometric model, which delineates the geometric boundaries and spatial relationships of geological bodies (e.g., strata, faults, intrusive bodies), provides an essential structural framework for attribute interpolation and stochastic simulation. This is because geological space is inherently heterogeneous and discontinuous; properties like density, chemical concentration, or seismic velocity are not solely functions of Euclidean distance but are strongly governed by the discrete geological structure defined by boundaries. Two points in close spatial proximity but residing on opposite sides of a significant geological boundary can exhibit vastly different properties. Therefore, the geometric model must serve as the primary conditioning framework during attribute modeling to ensure that property estimations respect the inherent geological discontinuities and spatial zonation. This integration ensures that the resulting attribute model not only honors the sampled data but also aligns with the underlying geological structure, thereby enhancing the reliability and practical utility of the model for MPM.

3.1 Spatial Interpolation

Spatial Interpolation serves as a fundamental tool for constructing 3D geological attribute models to fit a volumetric function from discrete and irregularly sampled data. The volumetric function can obtain the attribute value at each point in 3D space. Based on the selection of sampled data in fitting processes, interpolation methods are primarily categorized into global and local fitting. Global fitting methods, such as trend surface analysis and radial basis functions (RBFs), utilize all sampled data within the study area to approximate a single volumetric function describing regional trends. Conversely, local fitting methods, including inverse distance weighting (IDW) and Kriging, estimate values at unsampled locations using only sampled data from their neighborhood, thereby better capturing local spatial variability and complex geological structures.

3.1.1 Univariate Kriging

Kriging interpolation in geostatistics holds paramount importance in geosciences due to their statistical foundation. Unlike deterministic methods (e.g., IDW, spline interpolation), it treats a spatial attribute as the regionalized variable $Z(\boldsymbol{p})$ characterized by spatial autocorrelation (Krige, 1952; Matheron, 1963). A key advantage of Kriging is its ability to generate not only a predicted surface but also an associated Kriging variance surface, which quantifies the uncertainty or confidence of the prediction. Univariate Kriging interpolation estimates the value $\hat{Z}(\boldsymbol{p})$ at an un-sampled location $\boldsymbol{p}$ as a weighted linear combination of neighboring sample values $Z(\boldsymbol{p}_i)$ with weights λ_i, as follows:

$$\hat{Z}(\boldsymbol{p}) = \sum_{i=1}^{N} \lambda_i Z(\boldsymbol{p}_i) \ , \quad (1)$$

where N is the number of nearby samples used in the estimator. The spatial autocorrelation of regionalized variable is quantified by a semivariogram $\gamma(\boldsymbol{h})$, as follows:

$$(\boldsymbol{h}) = \frac{1}{2N(\boldsymbol{h})} \sum_{i=1}^{N(\boldsymbol{h})} [Z(\boldsymbol{p}_i) - Z(\boldsymbol{p}_i + \boldsymbol{h})]^2 \ , \quad (2)$$

where $N(\boldsymbol{h})$ represents the number of sampled point pairs with a lag vector $\boldsymbol{h}$ (with a distance and a direction). The relationship between the semivariogram $\gamma(\boldsymbol{h})$ and the covariance function $C(\boldsymbol{h})$ can be expressed as $\gamma(\boldsymbol{h}) = C(0) - C(\boldsymbol{h})$.

Ordinary Kriging (OK) provides the best linear unbiased estimator (BLUE) with zero expectation $\mathrm{E}[\hat{Z}(\boldsymbol{p}) - Z(\boldsymbol{p})] = 0$ and minimum variance $\min_{\boldsymbol{\lambda}} Var[\hat{Z}(\boldsymbol{p}) - Z(\boldsymbol{p})]$ for unsampled locations (Martínez-Cob, 1996; Song et al., 2025), therefore, the weights λ_i are determined by solving the following system:

$$\begin{cases} \sum_{i=1}^{N} \lambda_i \gamma(\boldsymbol{p}_i - \boldsymbol{p}_j) + \mu = \gamma(\boldsymbol{p} - \boldsymbol{p}_j), & j = 1, \dots, N \\ \sum_{i=1}^{N} \lambda_i = 1 \end{cases} \ , \quad (3)$$

where $\gamma(\boldsymbol{p}_i - \boldsymbol{p}_j)$ represents the semivariance between sampled points $\boldsymbol{p}_i$ and $\boldsymbol{p}_j$, $\gamma(\boldsymbol{p} - \boldsymbol{p}_j)$ is the semivariance between the unsampled location $\boldsymbol{p}$ and the sampled points $\boldsymbol{p}_j$, and μ is the Lagrange multiplier introduced to enforce the unbiasedness constraints. Figure 5 shows the Au grade model of a gold orebody interpolated by OK with three fitted semivariograms in different directions. The estimation variance can be expressed as follows:

$$\sigma^2(\boldsymbol{p}) = C(0) - 2\sum_{i=1}^{N} \lambda_i C(\boldsymbol{p} - \boldsymbol{p}_i) + \sum_{i=1}^{N}\sum_{j=1}^{N} \lambda_i \lambda_j C(\boldsymbol{p}_i - \boldsymbol{p}_j) . \quad (4)$$

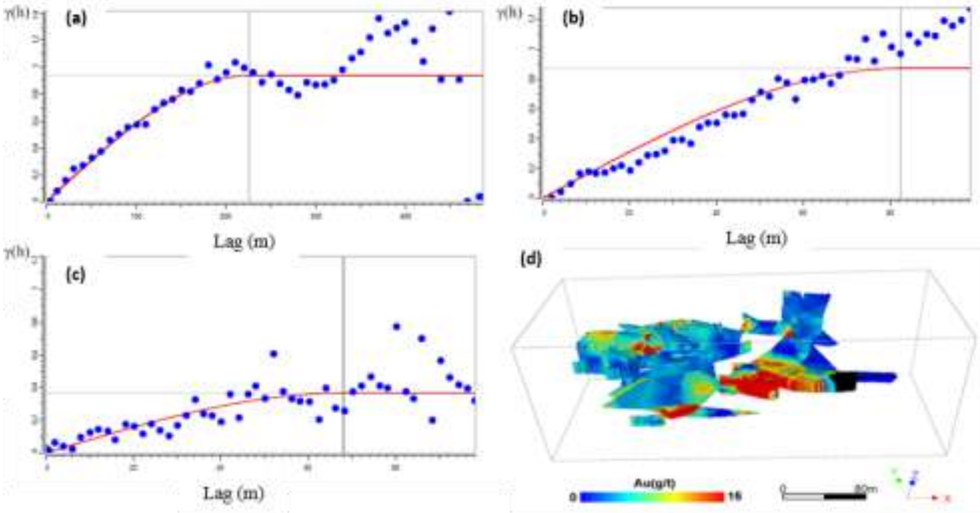

Fig. 5 Three semivariograms in (a) primary, (c) secondary, and (d) vertical directions and (d) the OK interpolated Au grade model of a gold orebody

Simple Kriging (SK) assumes the regionalized variable $Z(\boldsymbol{p})$ is second-order stationary with a known and constant mean m. SK directly models the residual $R(\boldsymbol{p}) = Z(\boldsymbol{p}) - m$. Because $E[R(\boldsymbol{p})] = 0$, SK estimator $\hat{R}(\boldsymbol{p}) = \sum_{i=1}^{N} \lambda_i R(\boldsymbol{p}_i)$ is automatically unbiased regardless of the weights, therefore, the weights λ_i are determined by solving the following equation:

$$\sum_{i=1}^{N} \lambda_i \gamma_R(\boldsymbol{p}_i - \boldsymbol{p}_j) = \gamma_R(\boldsymbol{p} - \boldsymbol{p}_j), \qquad j = 1, \dots, N \;, \quad (5)$$

where $\gamma_R()$ is the semivariogram of the residual regionalized variable $R(\boldsymbol{p})$.

The indicator Kriging (IK) is suited for categorical data with a regionalized indicator variable $0 \leq I(\boldsymbol{p};\ k) \leq 1$, which indicates the probability that a variable at an unsampled location $\boldsymbol{p}$ belongs to a specified category $k = 1, \dots, K$ (Amour et al., 2012; Chilès et al., 1993; Gunnink et al., 2021; Oh et al., 1999). The expected value of the indicator variable is the marginal probability:

$$\mathrm{E}[I(\boldsymbol{p}; k)] = \pi_k, \quad \sum_{k=1}^{K} \pi_k = 1 \;. \quad (6)$$

The weights $\lambda_i^{(k)}$ of IK estimator $\hat{I}(\boldsymbol{p}; k) = \sum_{i=1}^{N} \lambda_i^{(k)} I(\boldsymbol{p}_i; k)$ can be determined by solving the following OK system:

$$\begin{cases} \sum_{i=1}^{N} \lambda_i^{(k)} \gamma_{I,k}(\boldsymbol{p}_i - \boldsymbol{p}_j) + \mu^{(k)} = \gamma_{I,k}(\boldsymbol{p} - \boldsymbol{p}_j), \qquad j = 1, \dots, N \\ \sum_{i=1}^{N} \lambda_i^{(k)} = 1 \end{cases}, \quad (7)$$

where $\gamma_{I,k}()$ is the corresponding indicator semivariogram of the regionalized variable $I(\boldsymbol{p};k)$.

3.1.2 Cokriging

The bivariate form of cokriging (CK) can incorporate a secondary correlated variable $Z_2(\boldsymbol{p})$ (e.g., geophysical or geochemical data) to estimate the primary variable $Z_1(\boldsymbol{p})$ (Emery, 2012; Goovaerts, 2000), as follows:

$$\hat{Z}_1(\boldsymbol{p}) = \sum_{i=1}^{N_1} \lambda_i Z_1(\boldsymbol{p}_i) + \sum_{j=1}^{N_2} v_j Z_2(\boldsymbol{p}_j) \ , \quad (8)$$

where v_j is the weight for the secondary variable $Z_1(\boldsymbol{p}_j)$ at sampled point $\boldsymbol{p}_j$. The spatial cross-correlation of two regionalized variables are modeled by a cross-semivariogram $\gamma_{12}(\boldsymbol{h})$, as follows:

$$\gamma_{12}(\boldsymbol{h}) = \frac{1}{2N_{12}(\boldsymbol{h})} \sum_{i=1}^{N_{12}(\boldsymbol{h})} [Z_1(\boldsymbol{p}_i) - Z_1(\boldsymbol{p}_i + \boldsymbol{h})][Z_2(\boldsymbol{p}_i) - Z_2(\boldsymbol{p}_i + \boldsymbol{h})] \ , \quad (9)$$

where $N_{12}(\boldsymbol{h})$ represents the number of sampled point pairs with a lag vector $\boldsymbol{h}$. The weights of λ_i and v_j for the primary and secondary variables are determined by solving the following system:

$$\begin{cases} \sum_{i=1}^{N_1} \lambda_i \gamma_{11}(\boldsymbol{p}_i - \boldsymbol{p}_k) + \sum_{j=1}^{N_2} v_j \gamma_{12}(\boldsymbol{p}_j - \boldsymbol{p}_k) + \mu_1 = \gamma_{11}(\boldsymbol{p} - \boldsymbol{p}_k), & k = 1, \dots, N_1 \\ \sum_{i=1}^{N_1} \lambda_i \gamma_{12}(\boldsymbol{p}_i - \boldsymbol{p}_l) + \sum_{j=1}^{N_2} v_j \gamma_{22}(\boldsymbol{p}_j - \boldsymbol{p}_l) + \mu_2 = \gamma_{12}(\boldsymbol{p} - \boldsymbol{p}_l), & l = 1, \dots, N_2 \\ \sum_{i=1}^{N_1} \lambda_i = 1 & \\ \sum_{j=1}^{N_2} v_j = 0 & \end{cases} , (10)$$

where $\gamma_{11}(\boldsymbol{p}_i - \boldsymbol{p}_k)$ represents the semivariance of the primary variable $Z_1(\boldsymbol{p})$ between points $\boldsymbol{p}_i$ and $\boldsymbol{p}_k$, $\gamma_{12}(\boldsymbol{p}_j - \boldsymbol{p}_k)$ is the cross-semivariance of the primary and secondary variables between points $\boldsymbol{p}_j$ and $\boldsymbol{p}_k$, $\gamma_{22}(\boldsymbol{p}_j - \boldsymbol{p}_l)$ represents the semivariance of the secondary variable $Z_2(\boldsymbol{p})$ between points $\boldsymbol{p}_j$ and $\boldsymbol{p}_l$, and μ_1 and μ_2 are the Lagrange multipliers.

Spatial interpolation plays an indispensable role in building volumetric models. It directly enables: (1) ore grade interpolation, transforming sparse borehole assay data into a 3D volumetric model of element concentration for resource evaluation and mine planning; (2) resampling of geophysical fields, such as converting irregularly spaced gravity or magnetic survey measurements into a regular 3D voxel grid for integration with volumetric model and quantitative prediction of concealed orebodies; and (3) resampling of geochemical fields, creating 2D surface elemental distributions to link subsurface geochemical halos and alteration patterns associated with concealed mineralization. Thus, the selection and application of an appropriate spatial interpolation method, guided by data characteristics and geological understanding, is crucial for generating reliable 3D attribute models that underpin MPM.

3.2 Stochastic Simulation

While deterministic interpolation methods provide a single estimate of spatial attributes, they often fail to capture the full heterogeneity, complexity, and inherent uncertainty of subsurface geological properties. Stochastic simulation addresses this limitation by generating multiple, equally probable realizations of the spatial attribute distribution (Bai et al., 2022; Deutsch et al., 1993). Each realization honors the input sample data and reproduces spatial patterns (e.g., semivariogram, training image), providing a powerful framework for quantifying spatial attribute uncertainty. Compared to Kriging, stochastic modeling through random function theory can better reflect the heterogeneity and discontinuity of geological attribute distributions.

3.2.1 Sequential Gaussian Simulation (SGS)

SGS is designed for simulating continuous variables $Z(\boldsymbol{p})$ (e.g., ore grade, density) that can be normal-score transformed to a standard normal distribution $Y(\boldsymbol{p}) = G^{-1}(F(Z(\boldsymbol{p}))) \sim N(0, 1)$, where $F(z) = \mathrm{Prob}\{Z(\boldsymbol{p}) \leq z\} \sim U(0, 1)$ is the cumulative distribution function (CDF) of the original regionalized variable $Z(\boldsymbol{p})$, $G()$ is the standard Gaussian CDF, and $G^{-1}()$ is the inverse CDF of the standard Gaussian distribution. The core principle involves sequentially visiting each unsampled location (voxel) in the 3D grid, constructing a conditional cumulative distribution function (CCDF) based on neighboring original data and previously simulated values, and then randomly drawing a value from this CCDF (Bai et al., 2022; Grana et al., 2012; Haas et al., 1994; Nunes et al., 2010). The simulation proceeds sequentially by visiting each node along a random path and drawing a value form its local condition distribution. At each unsampled location $\boldsymbol{p}$ along the path, SK is performed using the normal-score data and previously simulated values to estimate the mean $\hat{Y}_{SK}(\boldsymbol{p})$ and variance $\sigma_{SK}^2(\boldsymbol{p})$ of the CCDF, assuming a multi-Gaussian model $N(\hat{Y}_{SK}(\boldsymbol{p}), \sigma_{SK}^2(\boldsymbol{p}))$, and the simulated value is computed as follows:

$$Y^{(l)}(\boldsymbol{p}) = \hat{Y}_{SK}(\boldsymbol{p}) + \sigma_{SK}(\boldsymbol{p}) \cdot G^{-1}(q), \quad (11)$$

where q is random quantile from $U(0, 1)$. After simulating all nodes in the normal score space, the inverse normal-score transform $Z^{(l)}(\boldsymbol{p}) = F^{-1}(G(Y^{(l)}(\boldsymbol{p})))$ is applied to obtain the simulated field in the original units, then one realization is produced. Different random paths are repeated to generate multiple equiprobable realizations.

3.2.2 Sequential Indicator Simulation (SIS)

SIS is designed for simulating categorical variables (e.g., lithofacies, rock types) or for generating uncertainty intervals for continuous variables by discretizing them into classes. It does not assume a Gaussian distribution; it is a non-parametric method (Liu et al., 2013). For each node along a random path, retrieving the neighborhood of original indicators and previously simulated category assignments, IK is performed to obtain $\hat{I}(\boldsymbol{p}; k)$, and the simulated value is assigned to the category whose indicator $\hat{I}(\boldsymbol{p}; k) \geq q$ first exceeds a random number $q \sim U(0, 1)$. After all unsampled grid nodes are simulated, one realization of the categorial field is obtained.

3.2.3 Multiple-point Statistics (MPS)

MPS borrows spatial patterns from training images (TIs), thereby better preserving curvilinear features (e.g., meandering channels, anastomosing lobes, fault networks) or high-order connectivity that are essential in geological heterogeneity (Guo et al., 2022; Hou et al., 2022; Strebelle, 2002). The TI embodies the target spatial patterns in a fully populated 3D grid which is a process-based model, an object-based model, or even a hand-drawn sketch, directly embedding expert geological knowledge. No explicit covariance or semivariogram function is involved in MPS; the spatial continuity is encoded entirely in the empirical distribution of patterns.

Let the attribute of interest be a categorical variable $S(\boldsymbol{p})$ taking K states, the ultimate goal in sequential simulation is to estimate the conditional probability distributions:

$$Prob(S(\boldsymbol{p}) = s_k | \, \boldsymbol{d}_n) \approx \frac{c_k(\boldsymbol{d}_n)}{c(\boldsymbol{d}_n)}, \quad k = 1, \dots, K, \quad (12)$$

where a data template includes n spatial vectors $\{\boldsymbol{h}_1, \boldsymbol{h}_2, \dots, \boldsymbol{h}_n\}$ defining a neighborhood geometry around a central location $\boldsymbol{p}$, and $\boldsymbol{d}_n$ is the data event which combines categorial values observed at the data template nodes given the current conditioning data. This probability is inferred directly from TIs by counting replicates of the data event $\boldsymbol{d}_n$. $c_k(\boldsymbol{d}_n)$ is number of such patterns in TIs where the central node value is s_k, and $c(\boldsymbol{d}_n)$ is number of patterns whose data event equals $\boldsymbol{d}_n$. The simulation proceeds voxel-by-voxel along a random path visiting all unsampled locations. At each location $\boldsymbol{p}$, the set of hard data and previously simulated values form the conditioning data event $\boldsymbol{d}_n$. The simulated value is assigned to the category whose cumulative probability exceeds a random number $q \sim U(0, 1)$.

3 Models

Data structures of 3D GMs comprise solid, volumetric, and hybrid models.

(1) Solid Model

The solid model represents 3D geological structures using combinations of points, lines, surfaces, and bodies, emphasizing their geometric shapes and topological relationships (Raiber et al., 2015; Wang et al., 2019; Zhang et al., 2023). It utilizes TINs to represent geological interfaces and assumes property homogeneity within a geological body. Solid model offers compact data volumes, facilitating visualization and spatial and topological queries of models, however, it struggles to express internal property changes within geological bodies, making its effective spatial analysis challenging.

(2) Volumetric Model

The volumetric model discretely subdivides 3D geological space using regular or irregular voxels, focusing on the spatial distribution of physical and chemical properties, such as element concentration, density, porosity, and permeability (Wang et al., 2017; Xie et al., 2025; Zhang et al., 2023). It is easily combined with geophysical and geochemical fields to realize the complementarity and mutual verification of geological settings. While exceling in spatial operations and analysis, volumetric model struggles to delineate accurate geological boundaries due to regular voxelization. Despite its large volume due to resolution concerns, 3D raster model is still a representative regular volumetric model in MPM, stored as a 3D array in computer, suitable for spatial overlay, correlation analysis, and statistical modeling. Irregular volumetric models, such as TPV and TEN, impose significant challenges for MPM overlay analysis due to computational intensity, while also necessitating the maintenance of complex topological relationships among voxels.

(3) Hybrid Model

The selection of data structure depends on specific needs of geosciences problem-solving. Given complexities of geological structures, it is usually necessary to integrate or interchange between two kinds of models, as shown in Figure 6. For instance, establishing the volumetric model for a geological body often relies on voxelization of its solid model, reconstructed using boundary surfaces, into 3D voxels, however, the result 3D volumetric model is categorial, within each geological body sharing an identical category.

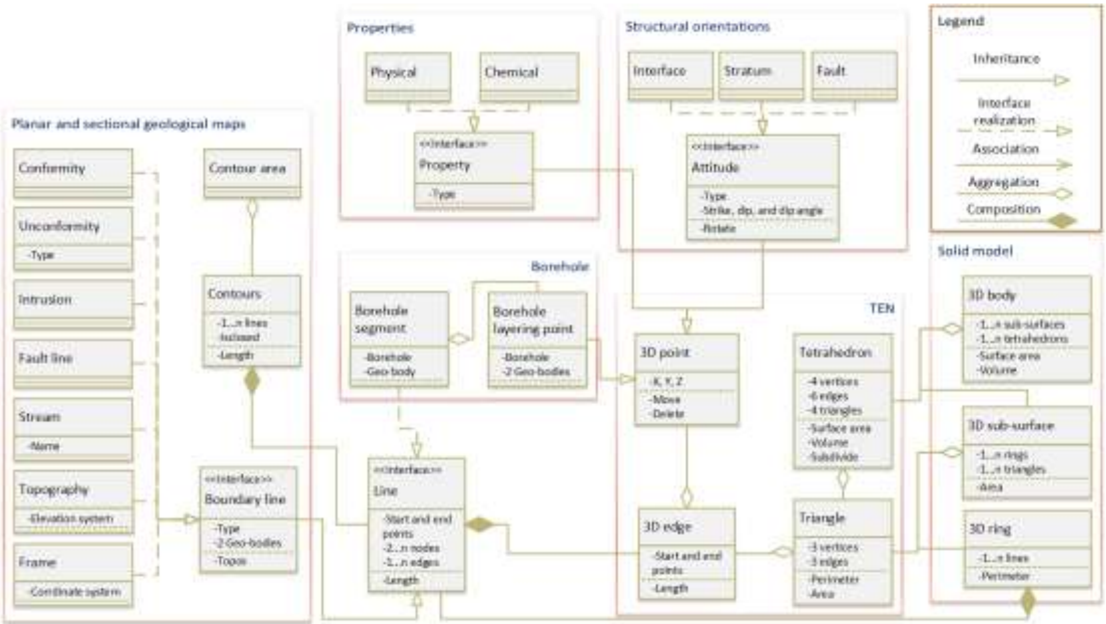

Fig. 6 A hybrid 3D model combining solid model with TEN reconstructed from boreholes, 2D planar and sectional geological maps, and physical and chemical properties

4 Spatial Analysis and Statistics

Spatial analysis and statistics methods for 3D GMs are crucial in solving challenges in geological study, e.g., the complexities of geological structures, lack of direct sampling data, comprehensive verifications of geophysical and geochemical explorations, and difficulties of spatial data mining, which provide essential tools for studying geological evolution in the deep subsurface space, deepening the comprehension of spatial distribution patterns of geological structures and guiding specific geosciences problem-solving. They also bridge the gaps of dimensionalities (2D or 3D) and types (qualitative or quantitative) in 3D MPM data. 3D GMs and their spatial analysis methods establish integrated 3D quantitative methods for locating concealed orebodies in MPM (Deng et al., 2022; Liu et al., 2003; Mao et al., 2016). As shown in Figure 7, for construction of geological ore-controlling variables, the commonly used spatial analysis methods include interpolation analysis, stochastic simulation, distance analysis, direction analysis, iso-surface analysis, gradient analysis, spatial autocorrelation analysis, and clustering analysis. When analyzing the relationship between mineralization and geological ore-controlling variables, cross-correlation analysis and spatial regression analysis are usually used.

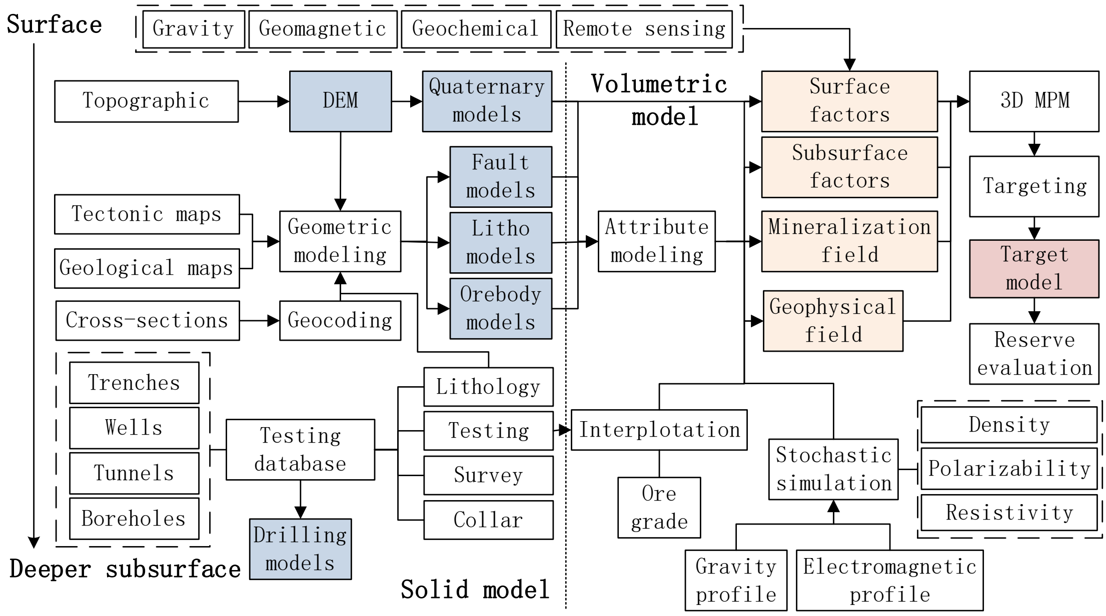

Fig. 7 Spatial analysis and statistics of 3D GMs in MPM

(1) Distance Analysis

In 3D MPM, distance analysis of geological bodies, such as faults, folds, or rocks, is often necessary to extract their morphological characteristics and quantifies the spatial influence of ore-controlling factors, by generating continuous distance fields (Behera et al., 2021; Fisher et al., 2013; Mao et al., 2020; Wang et al., 2019). When calculating the distance between the target voxel and a geological boundary, the distance is zero, negative, or positive if it on, insides, or outside the geological boundary, respectively.

(2) Direction Analysis

Direction analysis quantifies the spatial direction relationships between target voxels and geological bodies, thereby deriving predictive variables that constrain mineralization targeting by encoding the preferred orientation of ore-controlling structures (McLellan et al., 2008). The triple of {*Strike*, *Dip*, *Dip Angle*} is usually used to analyze the spatial direction relationship among geological bodies, which refers to the direction from the target voxel *O* to a source geological body. Spatial direction can also be qualitatively described by east/west, north/south, and up/down in three coordinate axes, therefore, it is divided into 27 categories through different coordinate quadrant combinations that include target voxel *O* itself.

(3) Spatial Clustering

Spatial clustering is to find clusters of objects such that the objects in a group will be similar (or related) to one another and different from (or unrelated to) the objects in other clusters. It serves to partition the subsurface into distinct clusters based on the similarity of multivariate attributes, thereby enabling the automatic identification of anomalous patterns, coherent geological domains, and potential mineralization-related signatures that are critical for defining exploration targets in MPM (Liu et al., 2023; Nagasingha et al., 2025; Yang et al., 2026). Spatial clustering is not only a stand-alone tool to get insight into geological variable distribution but also a preprocessing step for other spatial analysis and statistics methods. The procedure of spatial clustering is shown in Figure 8.

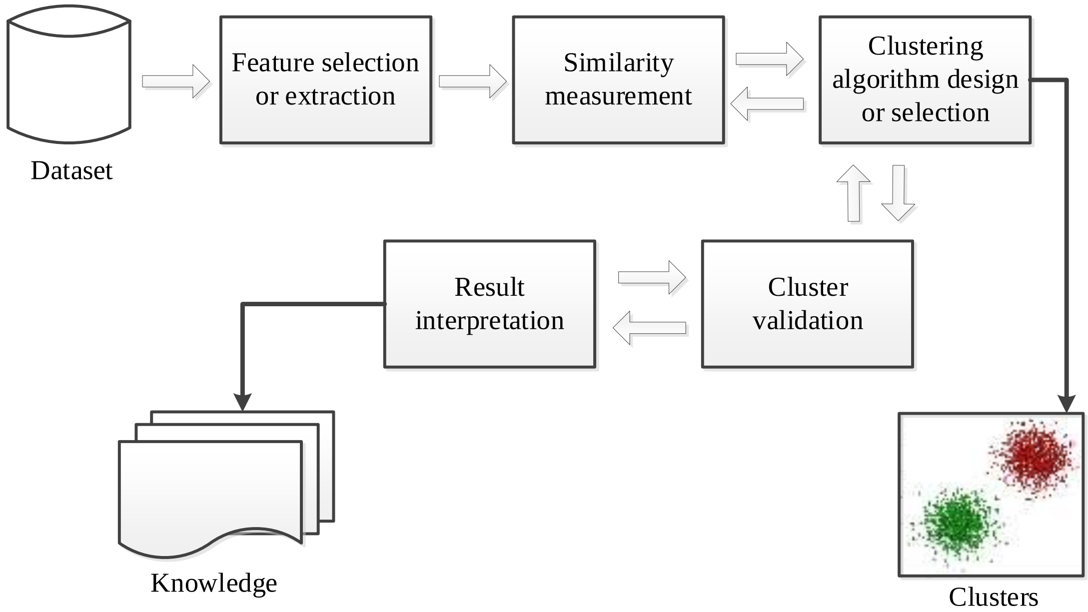

Fig. 8 Procedure of spatial clustering

(4) Spatial autocorrelation

Spatial autocorrelation reflects degree of correlation between an observed attribute x_i of the target voxel and the same attribute x_j of its N adjacent voxels. It quantifies the degree of spatial dependency and clustering patterns of a geological variable within a model, serving as a fundamental measure for understanding the inherent spatial structure of ore-controlling factors and as a critical prerequisite for subsequent spatial statistical inference in MPM (Huang et al., 2026). The measurement of spatial autocorrelation, such as the Moran's I and Geary's C statistics, can be expressed as a cross-product statistic between a spatial self-similarity matrix $\boldsymbol{w}_{ij}$ and an attribute self-similarity matrix $\boldsymbol{x}_{ij}$. For example, the local Moran's statistic $I(i)$ is calculated as follows:

$$I(i) = \frac{(x_i - \bar{x})\sum_{j=1}^{N} \boldsymbol{w}_{ij}(x_j - \bar{x})}{\frac{\sum_{j=1}^{N}(x_j - \bar{x})^2}{N}}, \quad (13)$$

where $\bar{x}$ is the mean attribute of the target voxel and its adjacent voxels.

(5) Spatial cross-correlation

For the spatial cross-correlation between two stochastic variables x and y, the local bivariate Moran's statistics $I_{xy}(i)$ is calculated as follows:

$$I_{xy}(i) = \frac{(x_i - \bar{x})\sum_{j=1}^{N} \boldsymbol{w}_{ij}(y_j - \bar{y})}{\frac{\sum_{j=1}^{N}(x_j - \bar{x})^2}{N}}, \quad (14)$$

where $\bar{x}$ and $\bar{y}$ are mean attributes of x and y, respectively. Spatial cross-correlation quantifies the degree of spatial association between an ore-controlling factor and a mineralization indicator across a 3D volume, thereby enabling the identification of spatially covarying exploration criteria and enhancing the MPM's predictive capability.

(6) Regression Analysis

Regression analysis is used to: (1) predict the value of a dependent variable based on the value of at least one independent variable; and (2) explain the impact of changes in an independent variable on the dependent variable. Dependent variable is the variable we wish to explain, such as ore grade/reserve, and independent variable is the variable used to explain the dependent variable, such as ore-controlling factors (Khammar et al., 2024; Li et al., 2026; Ramezanali et al., 2020; Xiao et al., 2022). For example, the multiple linear regression is to examine the linear relationship between one dependent variable y_i and K independent variables x_{ki} ($k = 1, 2, \ldots, K$) at a target voxel i, as follows:

$$y_i = \beta_0 + \beta_1 x_{1i} + \beta_2 x_{2i} + \cdots + \beta_K x_{Ki} + \varepsilon_i, \quad (15)$$

where ε_i is residual, and coefficients β_0, $\beta_1, \beta_2, \ldots, \beta_K$ of the multiple regression model can be estimated using sample data.

(7) Weight of Evidence (WofE)

For the categorial dependent variable, the WofE uses conditional probability theory to evaluate the spatial cross-correlation between the ore occurrence and ore-controlling evidence factors (Agterberg, 1991; Farahbakhsh et al., 2020; Wang et al., 2015; Zhang et al., 2023). However, various complex correlations between evidence factors can lead to the failure of WofE since it can only extract statistical correlations, instead of the spatial auto- and cross-correlations, between known deposits and evidence factors (Li et al., 2019; Wang et al., 2011). The joint conditional independence between evidence factors is a basic assumption of WofE, and the ore occurrence logarithmic posterior odds O at each voxel is expressed as:

$$\begin{cases} \ln(O) = b + \sum_{k=1}^{K} W_k \\ b = \ln\left(\dfrac{N(\boldsymbol{D})}{N(\boldsymbol{T}) - N(\boldsymbol{D})}\right) \end{cases}, \quad (16)$$

where $N(\boldsymbol{D})$ and $N(\boldsymbol{T})$ are voxel numbers of the ore-bearing set $\boldsymbol{D}$ and universal set $\boldsymbol{T}$, respectively, and W_k is the weight of evidence factor k, which equals to W_k^+, W_k^-, or zero when the evidence at current voxel is existent, non-existent or unknown, respectively. Therefore, the ore occurrence posterior probability P at each voxel is expressed as:

$$P = O/(1+O). \quad (17)$$

(8) Geographically Weighted Regression (GWR)

In conventional regression models, coefficients are the same at different voxels when assuming spatial stationary process. While spatial non-stationary process is more realistic, coefficients would be different at different voxels. If non-stationary process is modeled by stationary models, possible wrong conclusions might be drawn, or residuals of the model might be highly spatial auto-correlated. GWR is a local statistical technique to analyze spatial non-stationary variations in relationships, which is based on the “First Law of Geography”, that is, “everything is related with everything else, but closer things are more related.” GWR allows the relationships to vary over space, that is, β_0, β_1, $\beta_2, \ldots, \beta_K$ do not need to be the same everywhere, as follows:

$$y_i = \beta_{0i} + \beta_{1i} x_{1i} + \beta_{2i} x_{2i} + \cdots + \beta_{Ki} x_{Ki} + \varepsilon_i, \quad (18)$$

where coefficients β_{0i}, β_{1i}, $\beta_{2i}, \ldots, \beta_{Ki}$ now vary in terms of the voxel i, instead of remaining the same everywhere. GWR allows for the localized modeling of spatially non-stationary relationships between ore-controlling variables and mineralization, thereby providing a more nuanced and accurate characterization of ore-forming processes compared to traditional global regression models (Huang et al., 2024; Zhang et al., 2018).

Recent studies have demonstrated the efficacy of deep learning, particularly CNNs, in addressing the challenges faced by traditional MPM methods like WofE in complex metallogenic conditions (Ghezelbash et al., 2020; Zhang et al., 2021). CNNs not only capture auto-correlations within a massive 3D block model but also extract cross-correlations across multiple characteristic dimensions, allowing them to leverage spatial auto-auto-correlations and characteristic cross-correlations for improved classification models (Deng et al., 2022; Li et al., 2021; Zhang et al., 2023; Zheng et al., 2023). However, there is a large number of parameters to be estimated during the training process, which takes a lot of time associated with the use of 3D CNNs with deep network structures.

5 Conclusions

This review establishes that true utilities of 3D GMs are realized through its transformation into a quantitative spatial MPM framework via subsequent spatial analysis and statistics. By integrating geometric modeling (explicit and implicit) with attribute modeling (interpolation and stochastic simulation), and by applying spatial analytical techniques, such as distance, direction, gradient, and autocorrelation analysis, 3D GMs are converted into quantitatively characterized ore-controlling variables. Furthermore, the integration of these derived variables with spatial statistical techniques, including cross-correlation analysis, WofE, GWR, and emerging deep learning methods, provides a rigorous and evolving pathway for moving from qualitative visual interpretation to quantitative 3D MPM.

Despite these advancements, several critical limitations and avenues for future research remain. Firstly, while spatial correlation is routinely assessed, robust methods for quantitatively evaluating and modeling its variation across space, i.e., spatial heterogeneity or non-stationarity, are still needed to improve the geological predictivity and interpretability of spatial regression models in complex mineral systems. Secondly, to move from empirical, data-driven prediction to process-based understanding, a crucial long-term direction is the coupling of static 3D GMs with numerical simulation models. This integration would enable the kinetics simulation of ore-forming processes. Thirdly, the future of 3D predictive modeling lies in leveraging multimodal large language models (MMLMs), such as GPT, Gemini, and Qwen-VL. Future work should focus on introducing advanced MMLMs to autonomously learn complex, non-linear relationships between multi-source geological spatial variables and mineralization, thereby enhancing the objectivity, efficiency, and accuracy of concealed orebody target delineation.

Conflict of Interest

The authors declare no conflicts of interest.

Acknowledgements

The authors thank the MapGIS Laboratory co-constructed by the National Engineering Research Center of Geographic Information System of China and Central South University for providing MapGIS® software (Wuhan Zondy Cyber-Tech Co. Ltd., Wuhan, China).

Data Availability

The data generated or analyzed during this study are not publicly available due to privacy. Access may be granted upon reasonable request to the corresponding author, subject to approval from the relevant ethics committee or data owner.

Author Contributions

Methodology, Software, and Writing—original draft preparation: **Juxiang He**; Writing—original draft preparation: **Yongran Wang**; Software: **Xiaoxia Long**; Investigation: **Bicheng Wang**; Writing—review and editing: **Jinsong Yang**; Validation: **Kun Wu**; Conceptualization and Funding acquisition: **Or Aimon Brou Koffi Kablan**; Validation, Writing—review and editing, and Funding acquisition: **Lifang Wang**.

Founding

This study was supported by grants from the National Natural Science Foundation of China (Grant No. 42572387), the Hunan Provincial Natural Resource Science and Technology Planning Program (Grant No. HBZ20240144), and the Scientific Research Project of Geological Bureau of Hunan Province, China (Grant No. HNGSTP202301).

References

1. Agterberg, F. P. (1991). Combining indicator pattems in weights of evidence modeling for resource evaluation. *Nonrenewable Resources, 1*(1), 35-50.
2. Amour, F., Mutti, M., Christ, N., Immenhauser, A., Agar, S. M., Benson, G. S., . . . Kabiri, L. (2012). Capturing and modelling metre-scale spatial facies heterogeneity in a Jurassic ramp setting (Central High Atlas, Morocco). *Sedimentology, 59*(4), 1158-1189. doi:10.1111/j.1365-3091.2011.01299.x
3. Antepara, O., Balcázar, N., & Oliva, A. (2021). Tetrahedral adaptive mesh refinement for two-phase flows using conservative level-set method. *International Journal for Numerical Methods in Fluids*, *93*(2), 481-503. doi:https://doi.org/10.1002/fld.4893
4. Bai, T., & Tahmasebi, P. (2022). Sequential Gaussian simulation for geosystems modeling: A machine learning approach. *Geoscience Frontiers, 13*(1). doi:10.1016/j.gsf.2021.101258
5. Basson, I. J., Creus, P. K., Anthonissen, C. J., Stoch, B., & Ekkerd, J. (2016). Structural analysis and implicit 3D modelling of high-grade host rocks to the Venetia kimberlite diatremes, Central Zone, Limpopo Belt, South Africa. *Journal of Structural Geology, 86*, 47-61. doi:10.1016/j.jsg.2016.03.002
6. Behera, S., & Panigrahi, M. K. (2021). Mineral prospectivity modelling using singularity mapping and multifractal analysis of stream sediment geochemical data from the auriferous Hutti-Maski schist belt, S. India. *Ore Geology Reviews, 131*. doi:10.1016/j.oregeorev.2021.104029
7. Bérubé, C. L., Olivo, G. R., Chouteau, M., Perrouty, S., Shamsipour, P., Enkin, R. J., . . . Thiémonge, R. (2018). Predicting rock type and detecting hydrothermal alteration using machine learning and petrophysical properties of the Canadian Malartic ore and host rocks, Pontiac Subprovince, Québec, Canada. *Ore Geology Reviews, 96*, 130-145. doi:10.1016/j.oregeorev.2018.04.011
8. Bi, Z. F., Wu, X. M., Li, Z. L., Chang, D. K., & Yong, X. S. (2022). DeepISMNet: three-dimensional implicit structural modeling with convolutional neural network. *Geoscientific Model Development, 15*(17), 6841-6861. doi:10.5194/gmd-15-6841-2022
9. Calcagno, P., Chilès, J. P., Courrioux, G., & Guillen, A. (2008). Geological modelling from field data and geological knowledge: Part I. Modelling method coupling 3D potential-field interpolation and geological rules. *Physics of The Earth and Planetary Interiors, 171*(1–4), 147-157. doi: http://dx.doi.org/10.1016/j.pepi.2008.06.013
10. Caumon, G., Gray, G., Antoine, C., & Titeux, M.-O. (2013). Three-Dimensional Implicit Stratigraphic Model Building From Remote Sensing Data on Tetrahedral Meshes: Theory and Application to a Regional Model of La Popa Basin, NE Mexico. *IEEE Transactions on Geoscience and Remote Sensing, 51*(3), 1613-1621.
11. Chen, Y.-H., Li, A.-B., Lu, G.-N., & Xie, X.-L. (2023). An automated method for topology consistent processing of parallel geological cross-sections based on topology reasoning.

Computers & Geosciences, 180. doi:10.1016/ j.cageo.2023.105442

12. Chilès, J.-P., & Liao, H. T. (1993). Estimating the Recoverable Reserves of Gold Deposits: Comparison Between Disjunctive Kriging and Indicator Kriging. *Springer Netherlands*.
13. Cowan, E. J., Beatson, R. K., Ross, H. J., Fright, W. R., McLennan, T. J., Evans, T. R., . . . Titley, M. (2003). *Practical implicit geological modelling*. Paper presented at the 5th International Mining Geology Conference. <Go to ISI>://WOS:000238481700012
14. Cui, Y. A., Li, J. Q., Li, Y. C., Zhang, Z. T., & Du, J. (2026). Multiscale geometric digital twins of mine tunnels that integrate topological evolution and local reconstruction. *Tunnelling and Underground Space Technology, 169*, 21. doi:10.1016/j.tust. 2025. 107317
15. de la Varga, M., Schaaf, A., & Wellmann, F. (2019). GemPy 1.0: open-source stochastic geological modeling and inversion. *Geoscientific Model Development, 12*(1), 1-32. doi:10.5194/gmd-12-1-2019
16. Deng, H., Zheng, Y., Chen, J., Yu, S., Xiao, K., & Mao, X. (2022). Learning 3D mineral prospectivity from 3D geological models using convolutional neural networks: Application to a structure-controlled hydrothermal gold deposit. *Computers & Geosciences, 161*. doi:10.1016/j.cageo.2022. 105074
17. Deutsch, C. V., & Journel, A. G. (1993). GSLIB: Geostatistical Software Library and User's Guide.
18. Emery, X. (2012). Cokriging random fields with means related by known linear combinations. *Computers and Geosciences, 38*(1), 136-144. Retrieved from http://dx.doi. org/10.1016/j.cageo.2011.06.001
19. Farahbakhsh, E., Hezarkhani, A., Eslamkish, T., Bahroudi, A., & Chandra, R. (2020). Three-dimensional weights of evidence modelling of a deep-seated porphyry Cu deposit. *Geochemistry: Exploration, Environment, Analysis, 20*(4), 480-495. doi: 10.1144/geochem2020-038
20. Feather, W. G., Lim, H., & Knezevic, M. (2021). A numerical study into element type and mesh resolution for crystal plasticity finite element modeling of explicit grain structures. *Computational Mechanics, 67*(1), 33-55. doi: 10.1007/s00466-020-01918-x
21. Fisher, L. A., Cleverley, J. S., Pownceby, M., & MacRae, C. (2013). 3D representation of geochemical data, the corresponding alteration and associated REE mobility at the Ranger uranium deposit, Northern Territory, Australia. *Mineralium Deposita, 48*(8), 947-966. doi:10.1007/s00126-013-0463-6
22. Frings, K., von Hagke, C., Wellmann, F., Heim, E., de la Varga, M., Ortner, H., & Luijendijk, E. (2023). Constraining the 3-D Geometry of Fold-Thrust Belts Using Section Balancing vs. 3-D Interpolative Structural and Probabilistic Modeling. *τeκτonıκa, 1*(2), 54-75. doi:10.55575/tektonika2023.1.2.21
23. Galley, C. G., Lelièvre, P. G., & Farquharson, C. G. (2020). Geophysical inversion for 3D contact surface geometry. *Geophysics, 85*(6), K27-K45. doi:10.1190/geo2019-0614.1
24. García-Gil, A., Baquedano, C., Marazuela, M. A., Martínez-León, J., Cruz-Pérez, N., Hernández-Gutiérrez, L. E., & Santamarta, J. C. (2023). A 3D geological model of El Hierro volcanic island reflecting intraplate volcanism cycles. *Groundwater for Sustainable Development, 21*, 13. doi:10.1016/j.gsd.2023. 100936
25. Ghezelbash, R., Maghsoudi, A., & Carranza, E. J. M. (2020). Sensitivity analysis of prospectivity modeling to evidence maps: Enhancing success of targeting for epithermal gold, Takab district, NW Iran. *Ore Geology Reviews, 120*. doi:10.1016/j.oregeorev.2020. 103394
26. Goncalves, I. G., Kumaira, S., & Guadagnin, F. (2017). A machine learning approach to the

potential-field method for implicit modeling of geological structures. *Computers and Geosciences*, *103*, 173-182. doi:10.1016/j.cageo.2017.03.015

27. Goovaerts, P. (1997). *Geostatistics for Natural Recources Evaluation*. New York: Oxford University Press.
28. Goovaerts, P. (2000). Geostatistical approaches for incorporating elevation into the spatial interpolation of rainfall. *Journal of Hydrology, 228*(1–2), 113-129.
29. Grana, D., Mukerji, T., Dvorkin, J., & Mavko, G. (2012). Stochastic inversion of facies from seismic data based on sequential simulations and probability perturbation method. *Geophysics, 77*, 53. doi:10.1190/geo2011-0417.1
30. Grose, L., Ailleres, L., Laurent, G., Caumon, G., Jessell, M., & Armit, R. (2021). Modelling of faults in LoopStructural 1.0. *Geosci. Model Dev., 14*(10), 6197-6213. doi:10.5194/gmd-14-6197-2021
31. Grose, L., Ailleres, L., Laurent, G., & Jessell, M. (2021). LoopStructural 1.0: time-aware geological modelling. *Geoscientific Model Development*, *14*(6), 3915-3937. doi:10.5194/gmd-14-3915-2021
32. Gunnink, J. L., Pham, H. V., Essink, G., & Bierkens, M. F. P. (2021). The three-dimensional groundwater salinity distribution and fresh groundwater volumes in the Mekong Delta, Vietnam, inferred from geostatistical analyses. *Earth System Science Data, 13*(7), 3297-3319. doi:10.5194/essd-13-3297-2021
33. Guo, J., Wang, X., Wang, J., Dai, X., Wu, L., Li, C., . . . Jessell, M. W. (2021). Three-dimensional geological modeling and spatial analysis from geotechnical borehole data using an implicit surface and marching tetrahedra algorithm. *Engineering Geology, 284*,106047. doi:10.1016/j.enggeo.2021.106047
34. Guo, J., Wang, Z., Li, C., Li, F., Jessell, M. W., Wu, L., & Wang, J. (2022). Multiple-Point Geostatistics-Based Three-Dimensional Automatic Geological Modeling and Uncertainty Analysis for Borehole Data. *Natural Resources Research, 31*(5), 2347-2367. doi:10.1007/s11053-022-10071-6
35. Guo, J., Xu, X., Wang, L., Wang, X., Wu, L., Jessell, M., . . . Zheng, Y. (2024). GeoPDNN 1.0: a semi-supervised deep learning neural network using pseudo-labels for three-dimensional shallow strata modelling and uncertainty analysis in urban areas from borehole data. *Geosci. Model Dev., 17*(3), 957-973. doi:10.5194/gmd-17-957-2024
36. Haas, A., & Dubrule. (1994). Geostatistical inversion - a sequential method of stochastic reservoir modelling constrained by seismic data. *First Break, 12*, 561-569.
37. He, S., Cai, H., Liu, S., Xie, J., & Hu, X. (2021). Recovering 3D Basement Relief Using Gravity Data Through Convolutional Neural Networks. *Journal of Geophysical Research: Solid Earth, 126*(10). doi:10.1029/2021jb022611
38. Hillier, M., de Kemp, E., & Schetselaar, E. (2013). 3D form line construction by structural field interpolation (SFI) of geologic strike and dip observations. *Journal of Structural Geology, 51*, 167-179. doi:10.1016/j.jsg.2013.01.012
39. Hillier, M., Wellmann, F., Brodaric, B., de Kemp, E., & Schetselaar, E. (2021). Three-Dimensional Structural Geological Modeling Using Graph Neural Networks. *Mathematical Geosciences, 53*(8), 1725-1749. doi:10.1007/s11004-021-09945-x
40. Hillier, M., Wellmann, F., de Kemp, E. A., Brodaric, B., Schetselaar, E., & Bédard, K. (2023). GeoINR 1.0: an implicit neural network approach to three-dimensional geological modelling. *Geosci. Model Dev., 16*(23), 6987-7012. doi:10.5194/gmd-16-6987-2023
41. Hou, M. Q., Ye, Y. B., He, L., Han, B. J.,

Yang, L. W., & Luo, A. M. (2025). A refined hybrid method for 3D quaternary geological modeling and its application in coastal deposits. *Earth Science Informatics, 18*(2), 17. doi:10.1007/s12145-025-01891-0

42. Hou, W., Liu, H., Zheng, T., Chang, H., & Xiao, F. (2022). Extended GOSIM: MPS-Driven Simulation of 3D Geological Structure Using 2D Cross-Sections. *Earth and Space Science, 9*(6), e2021EA001801. doi:https:// doi.org/ 10.1029/2021EA001801
43. Houlding, S. W. (1994). 3D Geoscience Modeling: Computer Techniques for Geological Characterization. Berlin: Springer-Verlag.
44. Hu, X., Li, X., Yuan, F., Jowitt, S. M., Ord, A., Ye, R., . . . Durance, P. (2020). 3D Numerical Simulation-Based Targeting of Skarn Type Mineralization within the Xuancheng-Magushan Orefield, Middle-Lower Yangtze Metallogenic Belt, China. *Lithosphere, 2020* (1). doi:10.2113/2020/8351536
45. Huang, J. X., Deng, H., Mao, X. C., Wan, S. J., & Liu, Z. K. (2024). A Global-Local collaborative approach to quantifying spatial non-stationarity in three-dimensional mineral prospectivity modeling. *Ore Geology Reviews, 168*. doi:10.1016/j.oregeorev.2024. 106069
46. Huang, J. X., Wan, S. J., Deng, H., Zhang, B. Y., Huang, X. M., & Mao, X. C. (2026). Quantifying Spatial and Statistical Heterogeneities in the Relationships Between Mineralization and its Determinants for Quantile-Specific 3D Mineral Prospectivity Mapping. *Natural Resources Research*. doi:10.1007/s11053-025-10636-1
47. Irakarama, M., Laurent, G., Renaudeau, J., & Caumon, G. (2020). Finite Difference Implicit Structural Modeling of Geological Structures. *Mathematical Geosciences, 53*(5), 785-808. doi:10.1007/s11004-020-09887-w
48. Isaaks, E. H., & Srivastava, R. M. (1989). *An Introduction to Applied Geostatistics*. New York, USA: Oxford University Press.
49. Jessell, M. (2001). Three-dimensional geological modelling of potential-field. *Computers & Geosciences, 27*, 455–465.
50. Kaufmann, O., & Martin, T. (2008). 3D geological modelling from boreholes, cross-sections and geological maps, application over former natural gas storages in coal mines. *Computers & Geosciences, 34*(3), 278-290. doi:10.1016/j.cageo.2007.09.005
51. Khammar, F., Nykänen, V., Beier, C., & Niiranen, T. (2024). Translating mineral systems criteria into a prospectivity model for IOCG deposits in the Kolari region, Finland. *Ore Geology Reviews, 174*, 19. doi:10.1016/ j.oregeorev.2024.106326
52. Krige, D. G. (1952). A statistical approach to some basic mine valuation problems on the Witwatersrand, by D.G. Krige, published in the Journal, December 1951 : introduction by the author. *Journal of the Southern African Institute of Mining and Metallurgy, 52*(9), 201-203. doi:10.10520/AJA0038223X_4858
53. Lajaunie, C., Courrioux, G., & Manuel, L. (1997). Foliation fields and 3D cartography in geology: Principles of a method based on potential interpolation. *Mathematical Geology, 29*(4), 571-584. doi:http://dx.doi.org/ 10.1007/BF02775087
54. Lemon, A. M., & Jones, N. L. (2003). Building solid models from boreholes and user-defined cross-sections. *Computers and Geosciences, 29*(5), 547-555. Retrieved from http://dx.doi.org/10.1016/S0098-3004(03)000 51-7
55. Li, N., Yin, S., Li, C., Wang, Y., Xiao, K., Cao, R., . . . Li, C. (2023). An Uncertainty Analysis Method Based on a Globally Optimal Truth Discovery Model for Mineral Prospectivity Mapping. *Mathematical Geosciences*. doi:10.1007/s11004-023-10086-6
56. Li, S., Chen, J., Liu, C., & Wang, Y. (2021). Mineral Prospectivity Prediction via

Convolutional Neural Networks Based on Geological Big Data. *Journal of Earth Science, 32*(2), 327-347. doi:10.1007/s12583-020-1365-z

57. Li, X., Yuan, F., Zhang, M., Jowitt, S. M., Ord, A., Zhou, T., & Dai, W. (2019). 3D computational simulation-based mineral prospectivity modeling for exploration for concealed Fe-Cu skarn-type mineralization within the Yueshan orefield, Anqing district, Anhui Province, China. *Ore Geology Reviews, 105*,1-17. doi:10.1016/j.oregeorev.2018.12.003
58. Li, X. H., Ye, S. F., Yuan, F., Meng, D. Y., Zhang, J. J., Miao, X. H., . . . Li, Y. (2026). 3D mineral prospectivity modeling for concealed gold deposits based on 3DCNN and numerical modeling of ore-forming process in the Wuhe area, Anhui Province, China. *Ore Geology Reviews, 188*, 20. doi:10.1016/j.oregeorev. 2025.107075
59. Liu, H. M., Harris, J., Sherlock, R., Behnia, P., Grunsky, E., Naghizadeh, M., . . . Hill, G. (2023). Mineral prospectivity mapping using machine learning techniques for gold exploration in the Larder Lake area, Ontario, Canada. *Journal of Geochemical Exploration, 253*, 16. doi:10.1016/j.gexplo.2023.107279
60. Liu, J., li, X., Zhang, J., & Li, C. (2013). 3D Visualization for Detailed Sedimentary-Facies Modeling of Lishui Depression, East China Sea Basin. *Applied Mechanics and Materials, 442*,489-493. doi:10.4028/www.scientific.net/AMM.442.489
61. Liu, J. Q., Huang, X. B., Wu, C. L., Cheng, W. M., Xiang, W., & Xia, H. (2012). From the Area to the Point-Study on the Key Technology of 3D Geological Hazard Modeling in Three Gorges Reservoir Area. *Journal of Earth Science, 23*(2), 199-206. doi:10.1007/s12583-012-0246-5
62. Liu, L., & Peng, S. (2003). Prediction of hidden ore bodies by synthesis of geological, geophysical and geochemical information based on dynamic model in Fenghuangshan ore field, Tongling district, China. *Journal of Geochemical Exploration, 81*(1-3), 81-98. doi:10.1016/j.gexplo.2003.08.004
63. Mallet, J.-L. (2002). *Geomodeling*. New York: Oxford University Press.
64. Mallet, J.-L. (2004). Space-time mathematical framework for sedimentary geology. *Mathematical Geology, 36*(1), 1-32.
65. Mao, X., Zhang, B., Deng, H., Zou, Y., & Chen, J. (2016). Three-dimensional morphological analysis method for geologic bodies and its parallel implementation. *Computers & Geosciences, 96*, 11-22. doi:10.1016/j.cageo.2016.07.004
66. Mao, X. C., Zhang, W., Liu, Z. K., Ren, J., Bayless, R. C., & Deng, H. (2020). 3D Mineral Prospectivity Modeling for the Low-Sulfidation Epithermal Gold Deposit: A Case Study of the Axi Gold Deposit, Western Tianshan, NW China. *Minerals, 10*(3), 21. doi:10.3390/min10030233
67. Martelet, G., Calcagno, P., Gumiaux, C., Truffert, C., Bitri, A., Gapais, D., & Brun, J. P. (2004). Integrated 3D geophysical and geological modelling of the Hercynian Suture Zone in the Champtoceaux area (south Brittany, France). *Tectonophysics, 382*(1-2), 117-128. doi:10.1016/j.tecto.2003.12.009
68. Martínez-Cob, A. (1996). Multivariate geostatistical analysis of evapotranspiration and precipitation in mountainous terrain. *Journal of Hydrology, 174*(1), 19-35. doi: https://doi.org/10.1016/0022-1694(95)02755-6
69. Matheron, G. (1963). "Principles of geostatistics". *Economic Geology, 58*, 1246-1266.
70. McLellan, J. G., & Oliver, N. H. S. (2008). Discrete element modelling applied to mineral prospectivity analysis in the eastern Mount Isa Inlier. *Precambrian Research, 163*(1-2), 174-188. doi:10.1016/j.precamres.2007.08.018
71. Meyers, D., & Skinner, S. (1992). Surfaces

from Contours. *ACM Transactions on Graphics*, *11*(3), 228-258.
72. Nagasingha, L. M. A., Bérubé, C. L., & Ghanati, R. (2025). A generative neural network approach to uncertainty and risk-return analysis in mineral prospectivity modelling. *Ore Geology Reviews*, *186*. doi: 10.1016/j.oregeorev.2025.106844
73. Nunes, R., & Almeida, J. (2010). Parallelization of sequential Gaussian, indicator and direct simulation algorithms. *Computers & Geosciences*, *36*, 1042-1052. doi:10.1016/j.cageo.2010.03.005
74. Oh, W., & Lindquist, B. (1999). Image thresholding by indicator kriging. *IEEE Transactions on Pattern Analysis and Machine Intelligence*, *21*(7), P.590-602.
75. Pan, D. D., Xu, Z. H., Lu, X. M., Zhou, L. Q., & Li, H. Y. (2020). 3D scene and geological modeling using integrated multi-source spatial data: Methodology, challenges, and suggestions. *Tunnelling and Underground Space Technology*, *100*, 19. doi:10.1016/j.tust.2020.103393
76. Perrin, M., Zhu, B., Rainaud, J.-F., & Schneider, S. (2005). Knowledge-driven applications for geological modeling. *Journal of Petroleum Science and Engineering*, *47*(1-2), 89-104. doi:10.1016/j.petrol.2004.11.010
77. Raiber, M., Webb, J. A., Cendon, D. I., White, P. A., & Jacobsen, G. E. (2015). Environmental isotopes meet 3D geological modelling: Conceptualising recharge and structurally-controlled aquifer connectivity in the basalt plains of south-western Victoria, Australia. *Journal of Hydrology*, *527*, 262-280. doi:10.1016/j.jhydrol.2015.04.053
78. Ramezanali, A. K., Feizi, F., Jafarirad, A., & Lotfi, M. (2020). Geochemical Anomaly and Mineral Prospectivity Mapping for Vein-Type Copper Mineralization, Kuhsiah-e-Urmak Area, Iran: Application of Sequential Gaussian Simulation and Multivariate Regression Analysis. *Natural Resources Research*, *29*(1), 41-70. doi:10.1007/s11053-019-09565-7
79. Roberto, V., & Chiaruttini, C. (1999). Modeling and reasoning techniques in geologic interpretation. *IEEE Transactions on Systems Man and Cybernetics Part a-Systems and Humans*, *29*(5), 460-473. doi:10.1109/3468.784173
80. Schneider, T., Hu, Y., Gao, X., Dumas, J., Zorin, D., & Panozzo, D. (2022). A Large-Scale Comparison of Tetrahedral and Hexahedral Elements for Solving Elliptic PDEs with the Finite Element Method. *ACM Trans. Graph.*, *41*(3), Article 23. doi:10.1145/3508372
81. Si, H. (2015). TetGen, a Delaunay-Based Quality Tetrahedral Mesh Generator. *ACM Trans. Math. Softw.*, *41*(2), Article 11. doi:10.1145/2629697
82. Song, Y. Q., Tsai, F. T. C., Minsley, B. J., & Kress, W. H. (2025). Multi-lithofacies alluvial characterization via airborne electromagnetic-borehole fusion using ordinary interval kriging and geologic constraints. *Journal of Hydrology*, *663*, 18. doi:10.1016/j.jhydrol.2025.134209
83. Strebelle, S. (2002). Conditional simulation of complex geological structures using multiple-point statistics. *Mathematical Geology*, *34*(1), 1-21. doi:10.1023/a:1014009426274
84. Tanaka, A. P. B., Borges, J. P. G., de Matos, G. C., Campos, M. T. R., Cunha, B. M., de Souza, R. B., . . . Lima, A. P. M. (2022). Fault-related fracture modeling in a pre-salt lacustrine carbonate reservoir from Santos Basin, offshore Brazil: Predicting preferential fluid flow paths using 3D geological and flow simulation models. *Marine and Petroleum Geology*, *135*, 7. doi:10.1016/j.marpetgeo.2021.105392
85. Tian, Y. P., Xiao, S. K., Zhang, R., Weng, Z. P., Wu, X. C., & Wu, Y. J. (2024). Local dynamic update methods for 3D geological body structure model and voxel model. *Earth*

Science Informatics, *17*(1), 841-851. doi: 10.1007/s12145-023-01183-5

86. Wang, G., Li, R., Carranza, E. J. M., Zhang, S., Yan, C., Zhu, Y., . . . Yang, F. (2015). 3D geological modeling for prediction of subsurface Mo targets in the Luanchuan district, China. *Ore Geology Reviews*, *71*, 592-610. doi:10.1016/j.oregeorev.2015.03.002
87. Wang, G., Ma, Z., Li, R., Song, Y., Qu, J., Zhang, S., . . . Han, J. (2017). Integration of multi-source and multi-scale datasets for 3D structural modeling for subsurface exploration targeting, Luanchuan Mo-polymetallic district, China. *Journal of Applied Geophysics*, *139*, 269-290. doi:10.1016/j. jappgeo.2017.02.027
88. Wang, G., Zhang, S., Yan, C., Song, Y., Sun, Y., Li, D., & Xu, F. (2011). Mineral potential targeting and resource assessment based on 3D geological modeling in Luanchuan region, China. *Computers & Geosciences*, *37*(12), 1976-1988. doi:10.1016/j.cageo.2011.05.007
89. Wang, L. F., Wu, X. B., Zhang, B. Y., Li, X. F., Huang, A. S., Meng, F., & Dai, P. Y. (2019). Recognition of Significant Surface Soil Geochemical Anomalies Via Weighted 3D Shortest-Distance Field of Subsurface Orebodies: A Case Study in the Hongtoushan Copper Mine, NE China. *Natural Resources Research*, *28*(3), 587-607. doi:10.1007/s110 53-018-9410-7
90. Wu, L. (2004). Topological relations embodied in a generalized tri-prism (GTP) model for a 3D geoscience modeling system. *Computers & Geosciences*, *30*(4), 405-418. doi:10.1016/j.cageo.2003.06.005
91. Wu, Q., & Xu, H. (2003). An approach to computer modeling and visualization of geological faults in 3D. *Computers & Geosciences*, *29*(4), 503-509. doi:10.1016/s00 98-3004(03)00018-9
92. Wu, Q., & Xu, H. (2013). Three-dimensional geological modeling and its application in Digital Mine. *Science China Earth Sciences*, *57*(3), 491-502. doi:10.1007/s11430-013-46 71-9
93. Wu, Q., Xu, H., & Zou, X. (2005). An effective method for 3D geological modeling with multi-source data integration. *Computers & Geosciences*, *31*(1), 35-43. doi:10.1016/ j. cageo.2004.09.005
94. Xiao, F., Chen, W. L., Wang, J., & Erten, O. (2022). A Hybrid Logistic Regression: Gene Expression Programming Model and Its Application to Mineral Prospectivity Mapping. *Natural Resources Research*, *31*(4), 2041-2064. doi:10.1007/s11053-021-09918-1
95. Xie, M., Liu, B. L., Li, C., & Li, Y. H. (2025). Geo CNN-Trans: A Hybrid Deep Learning Framework for 3D Mineral Prospectivity Modeling. *Natural Resources Research*, 20. doi:10.1007/s11053-025-10612-9
96. Xu, C., & Dowd, P. A. (2003). Optimal construction and visualisation of geological structures. *Computers & Geosciences*, *29*(6), 761-773. doi:10.1016/s0098-3004(03)00026-8
97. Xu, Y., Li, Z., Xie, Z., Cai, H., Niu, P., & Liu, H. (2021). Mineral prospectivity mapping by deep learning method in Yawan-Daqiao area, Gansu. *Ore Geology Reviews*, *138*, 104316. doi:10.1016/j.oregeorev.2021.104316
98. Xue, Y., Sun, M., & Ma, A. (2004). On the reconstruction of three-dimensional complex geological objects using Delaunay triangulation. *Future Generation Computer Systems*, *20*(7), 1227-1234. doi:10.1016/j. future.2003.11.012
99. Yang, Y., Wen, L., Cao, C. J., Li, Y. H., Liu, B. L., Kong, Y. H., . . . Zhou, Z. L. (2026). HyperMinNet: A hypergraph-based framework incorporating high-order relationships for mineral prospectivity mapping. *Ore Geology Reviews*, *190*, 15. doi: 10.1016/j.oregeorev.2026.107157
100. Yusoff, I. M., & Yakubu, I. B. (2022). Three-Dimensional Tetrahedron Network (3D TEN) and Volumetric Geo- Objects (VGO) Data Model for Groundwater Simulation in

Bida Basin, Nigeria. *Geografia-Malaysian Journal of Society & Space*, *18*(4), 1-18. doi: 10.17576/geo-2022-1804-01

101. Zhang, B., Chen, Y., Huang, A., Lu, H., & Cheng, Q. (2018). Geochemical field and its roles on the 3D prediction of concealed ore-bodies. *Acta Petrologica Sinica*, *34*(2), 352-362. Retrieved from <Go to ISI>:// WOS: 000429429000012

102. Zhang, B., Du, L., Khan, U., Tong, Y., Wang, L., & Deng, H. (2023). AdaHRBF v1.0: gradient-adaptive Hermite–Birkhoff radial basis function interpolants for three-dimensional stratigraphic implicit modeling. *Geosci. Model Dev.*, *16*(13), 3651-3674. doi: 10.5194/gmd-16-3651-2023

103. Zhang, B., Xu, K., Khan, U., Li, X., Du, L., & Xu, Z. (2023). A lightweight convolutional neural network with end-to-end learning for three-dimensional mineral prospectivity modeling: A case study of the Sanhetun Area, Heilongjiang Province, Northeastern China. *Ore Geology Reviews*, *163*,105788. doi:https://doi.org/10.1016/j. oregeorev.2023.105788

104. Zhang, D. J., Ren, N., & Hou, X. H. (2018). An improved logistic regression model based on a spatially weighted technique (ILRBSWT v1.0) and its application to mineral prospectivity mapping. *Geoscientific Model Development*, *11*(6), 2525-2539. doi: 10.5194/gmd-11-2525-2018

105. Zhang, R. C., Li, H., Wu, M. F., & Wang, Y. Q. (2015). An automatic unified modeling method of geological object and engineering object based on tri-prism (TP). *Journal of Central South University*, *22*(4), 1419-1426. doi:10.1007/s11771-015-2659-7

106. Zhang, S., Carranza, E. J. M., Wei, H., Xiao, K., Yang, F., Xiang, J., . . . Xu, Y. (2021). Data-driven Mineral Prospectivity Mapping by Joint Application of Unsupervised Convolutional Auto-encoder Network and Supervised Convolutional Neural Network. *Natural Resources Research*, *30*(2), 1011-1031. doi:10.1007/s11053-020-09789-y

107. Zheng, Y., Deng, H., Wu, J., Wang, R., Liu, Z., Wu, L., . . . Chen, J. (2023). Space-associated domain adaptation for three-dimensional mineral prospectivity modeling. *International Journal of Digital Earth*, *16*(1), 2885-2911. doi:10.1080/17538947.2023.2241432

108. Zhong, D. H., Wang, Z., Zhang, Y. C., & Shi, M. N. (2018). Fluid-Solid Coupling Based on a Refined Fractured Rock Model and Stochastic Parameters: A Case Study of the Anti-Sliding Stability Analysis of the Xiangjiaba Project. *Rock Mechanics and Rock Engineering*, *51*(8), 2555-2567. doi:10.1007/s00603-017-1367-z